Feasibility study of a scalable optical interconnection network for massively parallel processing systems

Ahmed Louri and Stephen Furlonge

The theoretical modeling of a novel topology for scalable optical interconnection networks, called optical multimesh hypercube (OMMH), is developed to predict size, bit rate, bit-error rate, power budget, noise, efficiency, interconnect distance, pixel density, and misalignment sensitivity. The numerical predictions are validated with experimental data from commercially available products to assess the effects of various thermal, system, and geometric parameters on the behavior of the sample model. OMMH is a scalable network architecture that combines positive features of the hypercube (small diameter, regular, symmetric, and fault tolerant) and the mesh (constant node degree and size scalability). The OMMH is implemented by a free-space imaging system incorporated with a space-invariant hologram for the hypercube links and fiber optics to provide the mesh connectivity. The results of this work show that the free-space links can operate at 368 Mbits/s and the fiber-based links at 228 Mbits/s for a bit-error rate of 10^{-17} per channel. The predicted system size for 32 nodes in the OMMH is 4.16 mm $\times$ 4.16 mm $\times$ 3.38 cm. Using 16-bit, bit-parallel transmission per node, the system can operate at a bit rate of up to 5.88 Gbits/s for a size of 1.04 cm $\times$ 1.04 cm $\times$ 3.38 cm.

Key words: Hypercube, mesh, interconnection network, optical interconnect, parallel computing, scalability, space invariance, holographic grating, modeling.

1. Introduction

Two key issues and desirable features of interconnection networks for massively parallel processing systems are modularity (construction of a larger network from several smaller networks) and size scalability (the size of the network can be increased with nominal changes in the existing configuration with a comparable increase in performance).

Two popular point-to-point interconnection networks for parallel computers are the binary n cube, or hypercube, and the mesh network. The binary n cube has $N = 2^n$ nodes, each of node degree n. The attractiveness of the hypercube topology is its small diameter ($\log_2 N$), high connectivity, symmetric and regular nature, simple and efficient routing algorithms, and fault tolerance. A drawback of the hypercube, though, is its lack of scalability, which limits its use in building large-sized systems out of smaller-sized systems. The lack of scalability of the hypercube stems from the fact that the node degree is not bounded and varies as $\log_2 N$. This property makes the hypercube cost prohibitive for large N.

The mesh, because of its simple regular connection and constant node degree (4) is easily implemented and highly scalable. For a network size of N nodes, the minimal incremental size is approximately $\sqrt{N}$. The major limitation, however, is its large diameter ($\sqrt{N}$).

By combining the positive features of the hypercube (small diameter, regular, high connectivity, simple control and routing, symmetric, and fault tolerant) with a torus or wraparound mesh (constant node degree of 4 and size scalability) while circumventing their disadvantages (lack of scalability of the hypercube and large diameter of the mesh), a novel technology for scalable optical interconnection networks for massively parallel processing systems called the optical multimesh hypercube (OMMH) and its optical design methodology have been explored.[1–3]

In this paper, we present a model of a sample OMMH to determine its feasibility as a scalable optical interconnection network for massively parallel processing systems. By a model, we mean a

The authors are with the Department of Electrical and Computer Engineering, The University of Arizona, Tucson, Arizona 85721.

Received 14 June 1995; revised manuscript received 26 October 1995.

0003-6935/96/081296-13$06.00/0

small representation of the system to characterize the conceptual design and to predict the behavior of a laboratory prototype. This means that we analyze issues relating to packaging and alignment, issues relating to the optical geometry that have a direct impact on the system scalability and feasibility, issues relating to the holographic beam-steering element that implements the space-invariant fanout, the power requirements, interconnect medium (fiber and free space), and considerations for the receiver design. The analysis includes examination of power budget, bit rate, component size, pixel density, noise, link efficiency, interconnect distances, bit-error rate (BER), and misalignment sensitivity.

2. Optical Multimesh Hypercube Networks

In this section, we briefly define the structure of the OMMH and give some general features. More details can be found in Refs. 1–3.

A. Definition of Optical Multimesh Hypercube Networks

An OMMH is characterized by a triplet (l, m, n), where l represents the row dimension of a torus, m is the column dimension of the torus, and n is the dimension of a hypercube. For two nodes (i_1, j_1, k_1) and (i_2, j_2, k_2), where $0 \le i_1 < l$, $0 \le i_2 < l$, $0 \le j_1 < m$, $0 \le j_2 < m$, $0 \le k_1 < 2^n$, and $0 \le k_2 < 2^n$:

1. There is a torus link between two nodes if (1) $k_1 = k_2$ and (2) two components, i and j, differ by one in one component while the other component is identical.
2. There is also a torus link for the wraparound connection in the row if (1) $k_1 = k_2$ and (2) $i_1 = i_2$, $j_1 = 0$, $j_2 = m - 1$, or for the wraparound connection in the column if (1) $k_1 = k_2$ and (2) $j_1 = j_2$, $i_1 = 0$, $i_2 = l - 1$.
3. There is a hypercube link between two nodes if and only if (1) $i_1 = i_2$, (2) $j_1 = j_2$, and (3) k_1 and k_2 differ by one bit position in their binary representation.

Figure 1 shows a (2, 2, 3)-OMMH interconnection in which the solid lines represent hypercube links and the dashed lines represent torus links. A (2, 2, 3)-OMMH consists of $2 \times 2 \times 2^3 = 32$ nodes. Small filled circles represent nodes of the OMMH network. Both ends of torus links (dashed lines) are connected for wraparound connections if they have the same labels.

B. Size Scalability of the Optical Multimesh Hypercube Network

The size of the OMMH can grow without altering the number of links per node if the size of the torus is expanded, for example, by inserting hypercubes in the row or the column of the torus in Fig. 1. This feature allows the OMMH to be size scalable and modular, as it allows incremental expansion of small sizes compared with the doubling of size in the hypercube.

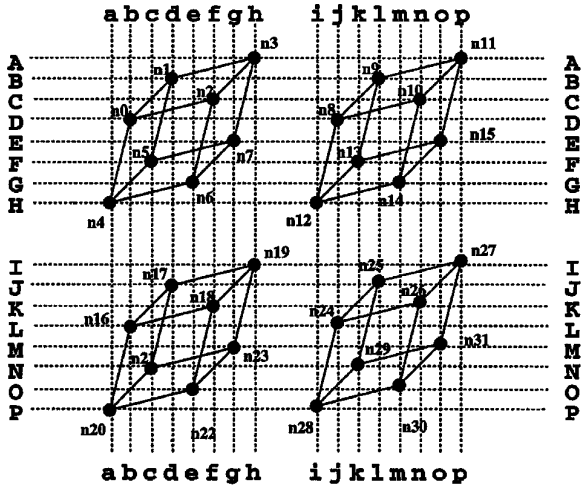

Fig. 1. Sample OMMH (2, 2, 3): four hypercubes, eight meshes, and 32 nodes.

3. Three-Dimensional Implementation of Optical Multimesh Hypercube Networks

The design method to implement the OMMH network is based on two optical technologies: space-invariant free-space optics for the hypercube links and fiber-based optics for the mesh links. The rationale for the design approach is that the use of space-invariant free-space optics would result in compact and simple building blocks that can be easily reproduced. We then use fiber optics to connect the basic building blocks because fiber optics are affordable scalable interconnects and wavelength-division multiplexing (WDM) could be used (1) to reduce the number of fibers as the network size grows and (2) to make a better utilization of the transmission capacity of the fiber and result in highly dense interconnections.

The motivations for the free-space implementation of the hypercubes in the OMMH are as follows: mass-production purposes for holographic space-invariant interconnections; a few simple processing steps are required for holograms whereas Si VLSI hypercubes easily require hundreds of processing steps (cost scales with processing steps); using the third dimension for free-space interconnections between nodes would mean no metal interconnections and more space for higher-bandwidth driver circuits.

The following is a list of components used in the OMMH.

A. Sources

In this paper, vertical-cavity surface-emitting lasers (VCSEL's) are used for the study as they are attractive light sources for optical interconnects because they are of low threshold current, low voltage (<2 V), high speed (10 GHz), high conversion efficiency, produce a single longitudinal mode, and emit a low divergence circularly symmetric, aberration-free beam well suited for efficient single-mode fiber coupling.[4–6] Moreover, their vertical geometry supports massive parallelism, and micro-optic integra-

tion in high-performance two-dimensional (2-D) arrays. Collimating or focusing lenslets can be formed on the substrate backside by etching processes that will minimize packaging costs. VCSEL's also have unique advantages for WDM applications.[7–9]

In addition, VCSEL-based systems are more manufacturable than spatial light modulator (SLM-) and self-electro-optic-effect-device-based systems. SLM's provide greater flexibility in heat removal because of the external optical power source but entails added complexity of imaging beams onto the SLM's. The difficulty of maintaining a wavelength with a few nanometers of tolerance makes the use of self-electro-optic-effect-device-based systems difficult.

B. Interconnect Medium

For freespace, holographic optical elements to distribute light to multiple detectors are studied. Additionally, fiber array bundles are used to meet the demand for enhanced information throughput and higher density while supporting wide bandwidth, low loss, low cross talk, light weight, small cross section, and immunity from electromagnetic interference.[10–12]

Because of the required compact and parallel nature of the overall system geometry, we use lenslet arrays, for free-space collimation and focusing, and fiber coupling. The use of arrays of microlenses is justified with the presumption that the system cost may be enhanced owing to the increased manufacturability and decreased alignment time.[13] Commercial lenslet arrays are available with individual lenslet diameters from 99 μm to 1 mm, *f*-numbers from 1 to 256, and focal lengths from 200 μm to 260 mm.

C. Detectors

P-I-N photodiode (PIN-PD) arrays are the most attractive for optical interconnects in terms of operating bias voltage, bandwidth, responsivity, noise, and 2-D array geometry.

They do not have an internal amplification mechanism; thus amplification is needed, which introduces additional noise. Transimpedance amplification circuits are commonly used in optical receivers because of the large dynamic range. Commercial PIN-PD 2-D arrays are available with high sensitivity in the visible to the near-infrared ranges with efficiencies of ≥70% and 3-GHz bandwidths.

4. Modeling a Sample Optical Multimesh Hypercube

Using the optical components identified in Section 3, we present, as an implementation example, a model for the physical implementation of the (2, 2, 3)-OMMH network shown in Fig. 1.

We first characterize the basic relations that are used in the analysis. Then we present the modeling of the free-space hypercube links and the fiber-based mesh links in the sample OMMH.

A. Basic Relations

1. *Free-Space Gaussian-Beam Propagation*

The propagation of a Gaussian beam in free-space is determined by

$$\omega^2(z) = {\omega_0}^2\left[1 + \left(\frac{\lambda z}{\pi {\omega_0}^2}\right)^2\right], \tag{1}$$

where $\omega(z)$, ω_0, and z represent the spot radius of the beam front at a distance z from the beam waist ω_0, where z is measured along the propagation axis at wavelength λ.

The propagation of a Gaussian beam through a microlens is described by

$$d1 = f + \frac{\omega_{01}}{\omega_{02}}\left[f^2 - \left(\frac{\pi}{\lambda}\,\omega_{01}\omega_{02}\right)^2\right]^{1/2},$$
$$d2 = f + \frac{\omega_{02}}{\omega_{01}}\left[f^2 - \left(\frac{\pi}{\lambda}\,\omega_{01}\omega_{02}\right)^2\right]^{1/2}, \tag{2}$$

where f is the focal length of the lens, ω_{01} and ω_{02} are the beam waists, and $d1$ and $d2$ are the respective distances of the waists from the lens.

2. *Diameter of the Microlens*

The diameter of the microlens, D_l, is determined by the divergence of the source radiation, the source-to-microlens distance, $d1$, and the amount of clipping of the Gaussian beam at the microlens. This amount is expressed by the clipping ratio, $k_l = r_l/\omega_l$, where r_l and ω_l represent the radius of the microlens and the radius of the spot size at the microlens, respectively. When $k_l = 2.12$, only 0.1% of the power is lost.[13]

3. *Optimum Coupling to a Fiber*

The mode propagating in the fiber can be approximated by a Gaussian beam and described through a mode radius ω_f. For optimum coupling into the fiber, this mode radius is slightly larger than the fiber core radius and is estimated by[14]

$$\frac{\omega_f}{a} = 0.65 + (1.619/V^{1.5}) + (2.879/V^6), \tag{3}$$

$$V = \left[\frac{2\pi a}{\lambda}\,({n_1}^2 - {n_2}^2)^{1/2}\right] = \frac{2\pi a}{\lambda}\,\mathrm{NA}, \tag{4}$$

where n_1 is the core index, n_2 is the cladding index, a is the core radius, and NA is the numerical aperture of the fiber. For single-mode operation, $V \leq 2.405$, which implies that $\omega_f/a \approx 1.1$.

B. Thermal Considerations for the Vertical-Cavity Surface-Emitting Lasers

A major concern for VCSEL transmitters is power dissipation. To avoid turn-on delays, the laser must be biased above threshold. The electrical power

used in getting to threshold produces little light, and thus it is considered to be wasted. This electrical power is dissipated as heat, P_{dissip}, where

$$P_{\text{dissip}} \approx P_{\text{th}} + \frac{P_l(1 - \eta_{\text{EO}})}{\eta_{\text{EO}}}, \tag{5}$$

$P_{\text{th}} = I_{\text{th}}V_{\text{th}}$, and I_{th} and V_{th} are the threshold current and the voltage, respectively. P_l is the optical output power, and η_{EO} is the electro-optical power-conversion slope efficiency in units of $\text{mW}_{\text{opt}}/\text{mW}_{\text{elec}}$. With $P_l = 0.8$ mW, $\eta_{\text{EO}} = 20\%$, $P_{\text{th}} = 16$ mW, and a maximum cooling capability of the system at 1 W/cm^2,[15] we are limited to a pixel density of $\approx$52 $\text{pixels}/\text{cm}^2$. A graph of pixel density versus the output laser power when a typical threshold power of 16 mW is used is shown in Fig. 2(a).

C. Receiver Design Considerations

The fraction of power that falls on a detector of radius r with beam-spot radius ω is given by

$$\eta_{\text{cd}} = 1 - \exp\left(\frac{-2r^2}{\omega^2}\right). \tag{6}$$

The detector current is given by

$$i_d = \frac{q\eta_d P_d}{h\nu}, \tag{7}$$

where q is the charge on the electron, η_d is the external differential quantum efficiency of the detector, P_d is the optical power incident upon the detector, and $h\nu$ is the energy per photon.

The average optical power required from a source for driving a receiver to obtain a desired BER is given by[16]

$$P_l = \frac{1 + r}{1 - r} Q \frac{hc}{\lambda q} \langle i_{\text{NA}}^2 \rangle^{1/2} \left(\frac{N}{\eta_{\text{sys}}\eta_d}\right), \tag{8}$$

where r is the ratio of current to the detector in the low-illumination state relative to the high-illumination state, Q is a parameter from communication theory that assumes Gaussian statistics for the detection process, $\langle i_{\text{NA}}^2 \rangle^{1/2}$ is the rms current noise generated by the detector and preamplifier circuit, and N is the system fan-out. For BER = 10^{-17}, Q = 8.6. A graph of the average optical power required from the laser for driving the receiver as a function of the bit rate is shown in Fig. 2(b), in which a return-to-zero (RZ) coding format is used for both the free-space and the fiber links.

The noise current is calculated from the parameters given in Table 1. These parameters are taken from Ref. 17. The values of I_2, I_3, and I_f are weighting functions for a RZ coding format for a GaAs metal-semiconductor field-effect-transistor (FET) transimpedance receiver. The noise current $\langle i_{\text{NA}}^2 \rangle$ is given by

$$\langle i_{\text{NA}}^2 \rangle = \frac{4kT}{R_f} I_2 B + 2qI_L I_2 B + \frac{4kT\Gamma}{g_m} (2\pi C_T)^2 f_c I_f B^2 + \frac{4kT\Gamma}{g_m} (2\pi C_T)^2 I_3 B^3, \tag{9}$$

where B is the bit rate, R_f is the feedback resistance, I_L is the total leakage current, g_m is the FET transconductance, C_T is the total input capacitance, f_c is the

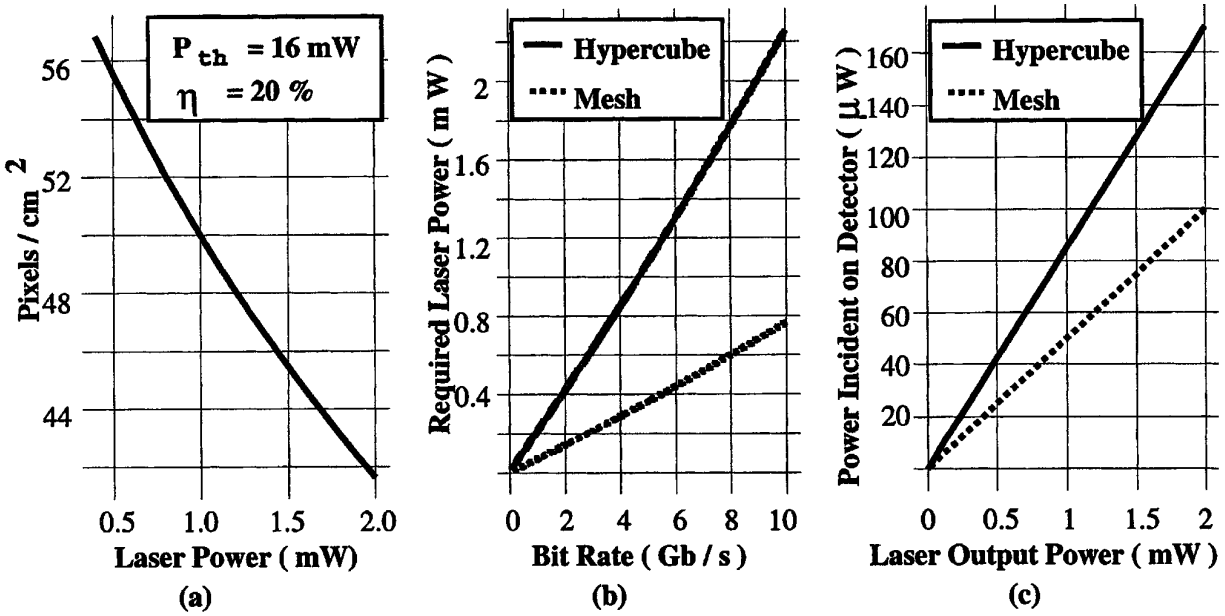

Fig. 2. (a) Pixel density versus output laser power, (b) required laser power to achieve a desired bit rate, (c) power incident upon detector P_d versus laser output power P_l. Gb/s, gigabits per second.

Table 1. Receiver Design Parameters

Receiver Design Parameter	Symbol	Value
Temperature	T	300 °K
Feedback resistance	R_f	1 kΩ
Gate-to-source capacitance	C_{gs}	0.35 pF
Gate-to-drain capacitance	C_{gd}	75 fF
Stray capacitance	C_f	0.75 pF
Photodetector capacitance	C_d	14 fF
Contrast ratio	r	0.1
FET noise parameter[a]	Γ	1.1
FET transconductance	g_m	40 mS
$1/f$ noise-corner frequency	f_c	15 GHz
Total leakage current	I_L	1 nA
Weighting function	I_2	0.4
Weighting function	I_3	0.04
Weighting function	I_f	0.0984
Detector quantum efficiency	η_d	0.877
Detector responsivity	R	0.6 A/W
Voltage	V	4 V

[a]FET, field-effect transistor.

$1/f$ noise-corner frequency of the FET, Γ is the FET noise parameter, k is Boltzmann's constant, and T is the temperature.

The speed of a detector is limited by the diffusion of carriers, the absorption depth of light in the material, and the capacitance of the depletion region. This capacitance requires time for charging by the photocarriers. A minimum voltage required by the receiver's input electronics must be reached, and the required optical power[18] is thus

$$P_d = \frac{E_{sw}}{\tau} = \frac{C_d V}{\tau R}, \tag{10}$$

where

$$R = \frac{\eta_d \lambda}{hc} = \frac{\eta_d \lambda(\mu m)}{1.2424},$$

V is the required voltage, E_{sw} is the switching energy, R is the detector responsivity, τ is the rise time, h is Planck's constant, and c is the speed of light.

A typical detector responsivity of 0.6 implies that $\eta_d = 0.877$, and from Eq. (13), with GaAs ($\alpha = 0.8/\mu m$, $\epsilon = 1.17E - 10$ F/m), the maximum thickness of the detector's depletion region is 2.62 μm. Thus, for a detector with a radius of 10 μm, the capacitance must be 14 fF ($C_d = \epsilon A/d$) where A and d are the detector's area and thickness, respectively. A graph of the bit rate versus the detector capacitance is shown in Fig. 3(a). The bit rate is limited by the capacitance of the device. A graph of the switching energy versus the total capacitance is shown in Fig. 3(b). The required switching energy increases with increasing capacitive effects.

D. Modeling the Free-Space Links in the Optical Multimesh Hypercube

The design methodology for the free-space hypercube links can be found in Ref. 1. Basically the nodes are partitioned into two sets such that any two nodes in the same set do not have a direct link. We call the two sets plane L and plane R. The conceptual view of the model for the sample OMMH is shown in Fig. 4. For clarity, the free-space and the fiber links are shown separately. A hybrid imaging system is used to provide the connectivity with a space-invariant hologram between plane L and plane R, as shown in Fig. 5. A space-invariant optical

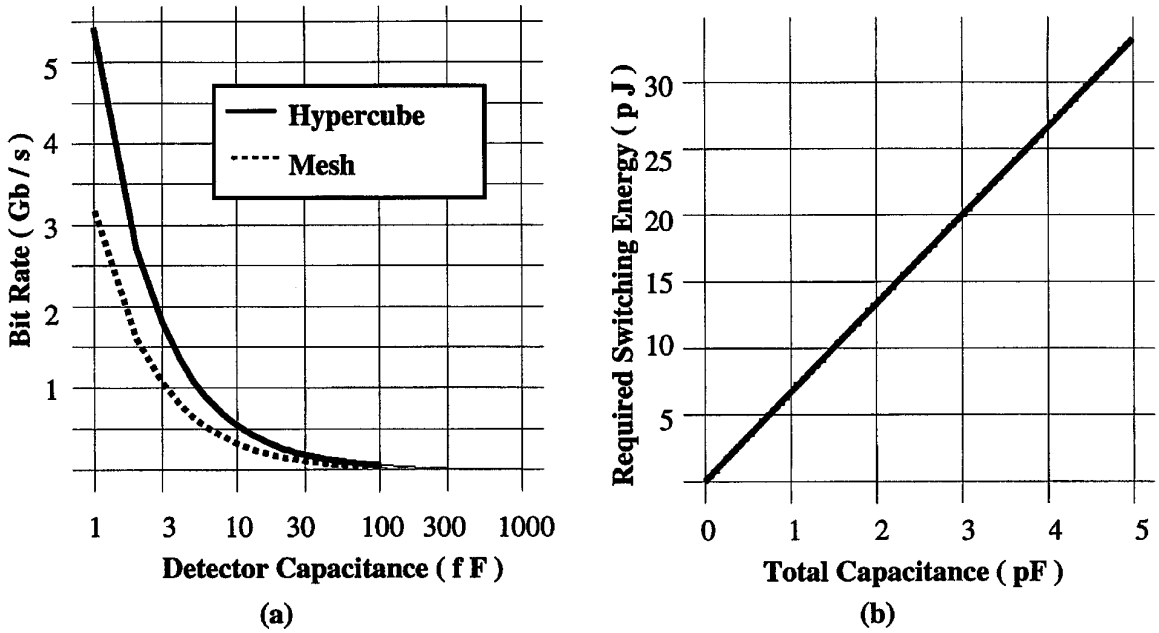

Fig. 3. (a) Bit rate versus capacitive effects at the receiver, (b) required switching energy versus capacitance at the receiver.

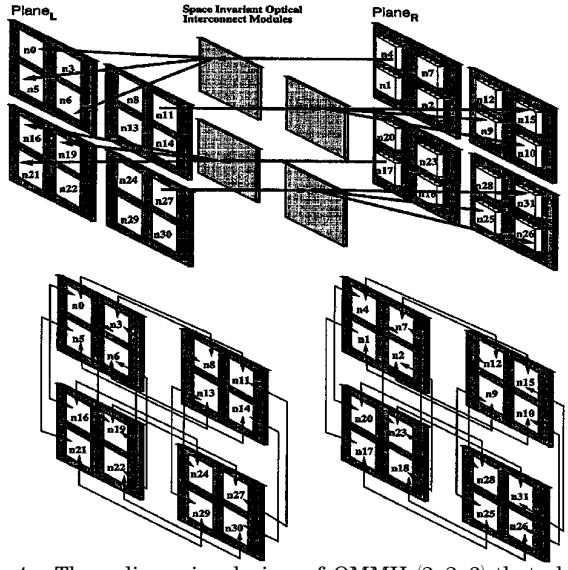

Fig. 4. Three-dimensional view of OMMH (2, 2, 3) that shows plane L and plane R interconnected by four space-invariant optical interconnection modules. The free-space links (top) are shown separated from the mesh links (bottom) for clarity.

interconnection module consists of a hybrid imaging system and a space-invariant hologram. The use of hybrid imaging systems has been proposed and demonstrated in Refs. 13 and 19. The setup combines $4 - f$ imaging with lenslet arrays. Lenslet arrays l_1 and l_2 have the tasks of reducing the numerical aperture of beams from the VCSEL's and providing tight focusing in the detector array. It is therefore possible to use imaging lenses L1 and L2 with relatively large f-numbers. This results in a significant reduction of the aberrations,[20] but at the same time this makes the system more sensitive to misalignment, and the larger the f-number, the smaller the angles of the diffracted orders from the hologram.

1. Beam Propagation through the Model

In Fig. 5, assume that the array of VCSEL diodes has an output window radius r_s and a laser-to-laser separation of ρ_s, microlens array $l1$ for collimation with individual lens diameter D_l and focal length f_l, microlens array $l2$ for focusing onto the detector

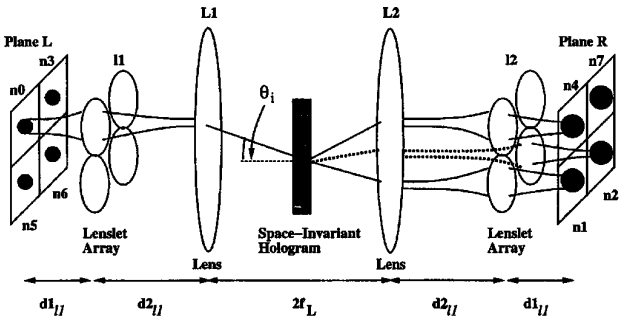

Fig. 5. Model for one hypercube that shows one space-invariant optical interconnection module.

array with focal length f_l and individual lens radius r_l, and light at wavelength λ_1. The array of photodetectors has an individual detector radius r_d and a detector-to-detector spacing of ρ_d. Lenses L1 and L2 have focal lengths f_L with diameter D_L and f-number $(f/\#)_L$. Because the system is symmetrical, lenses L1 and L2 are identical. Similarly, $l1$ and $l2$ are identical.

It is assumed that the laser emits a circular Gaussian beam. The radius of the beam near the laser facet is taken to be the beam waist ω_0. Let $d1_{l1}$ be the VCSEL source-to-lens-$l1$ distance and ω_{l1} be the radius of the beam incident upon the lens. Using Eqs. (1) and (2) and $k = 2.12$, we obtain the graphs below. A graph of the beam-spot diameter incident upon lens $l1$ versus the interconnect distance $d1_{l1}$ is shown in Fig. 6(a). The dependence of the beam-spot radius ω_{l1} on the focal length f_l is graphed in Fig. 6(b). A graph of the interconnect distance $d1_{l1}$ versus the focal length of lens $l1$ is shown in Fig. 7(a) for different values of the ratio ω_0/ω_{02}.

The distance $d2_{l1}$ from lens $l2$ to lens L1 can be calculated from Eqs. (2). Also, a graph of the interconnect distance $d2_{l1}$ versus f_l is shown in Fig. 7(b) for different values of the ratio ω_0/ω_{02}.

From the geometry, to avoid stray light into the other hypercubes, the focal length of lens L1 is

$$f_L = (f/\#)_L(3\rho_s + D_l), \tag{11}$$

where D_l is the diameter of lens $l1$.

The collimated beams are focused by lens L1 to the hologram plane where fan-out to the diffracted orders occur. Lens L2 then redirects the diffracted orders to lenslet array $l2$ for focusing to the appropriate detectors. Because the system is symmetrical, the distance from lens L2 to lens $l1$ is $d2_{l1}$ and from lens $l2$ to the detector is $d1_{l1}$.

2. Optical Efficiency of the Free-Space Links

The optical system efficiency η_{sys} of an optical interconnect is defined as the ratio of the power incident upon the detector, P_d, to the power emitted by the laser, P_l:

$$\eta_{sys} = P_d/P_l. \tag{12}$$

The total optical link efficiency is

$$\eta_{tot} = \eta_l \eta_c{}^2 \eta_h \eta_{cd} \eta_d, \tag{13}$$

where

$$\eta_d = 1 - \exp(-\alpha d),$$

η_l is the differential quantum efficiency of the laser diode, η_c is the coupling efficiency of the lenses, η_h is the efficiency of the hologram, η_{cd} is the fraction of

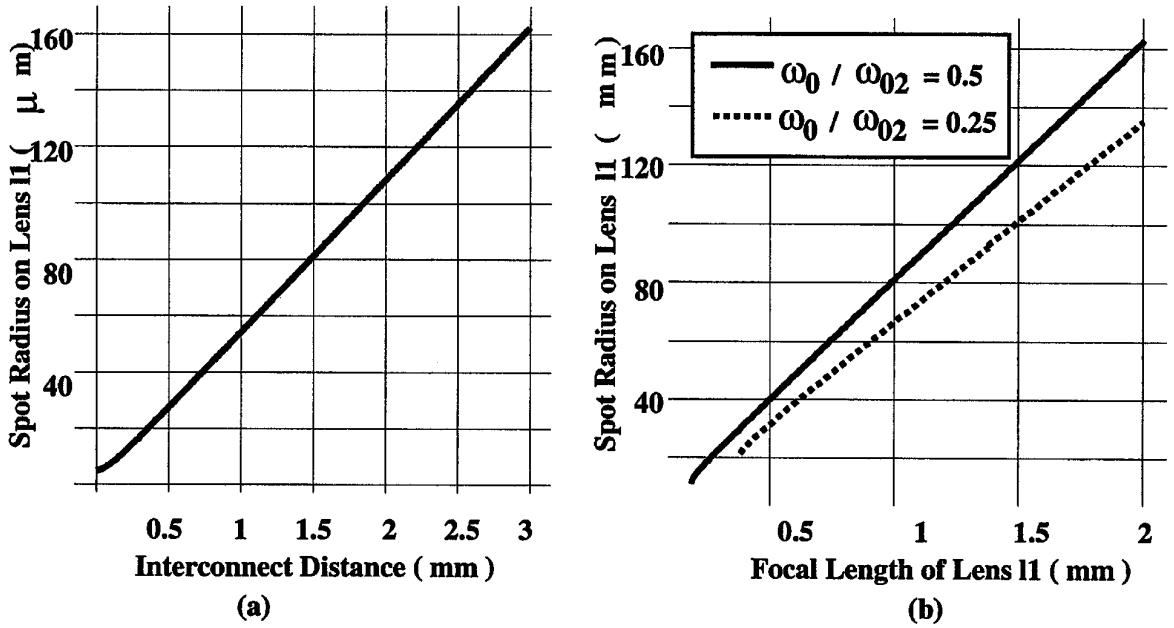

Fig. 6. (a) Beam-spot radius on lens $l1$ versus interconnect distance $d1_{l1}$, (b) beam-spot radius on lens $l1$ versus focal length f_l of lens $l1$.

power that falls on a detector of a given radius and beam-spot size, η_d is the photodetector quantum efficiency, α is the absorption coefficient, and d is the thickness of the detector active region.

We assume that the diffraction efficiency of the hologram (for each fan-out beam) is independent of the fan-out F. This has been shown to be approximately correct by several research groups.[21] Thus the efficiency of each diffracted beam from the hologram should be $\approx\eta_h/5$.

3. *Hologram Considerations*

The beam steering of the space-invariant hologram obeys the grating equation,

$$\Lambda(\sin\theta_d - \sin\theta_i) = m\lambda, \tag{14}$$

where θ_d, θ_i, Λ, λ, and m denote the diffracted angle, incident angle, grating period, wavelength, and diffraction order, respectively, and angles are measured against the optical axis.

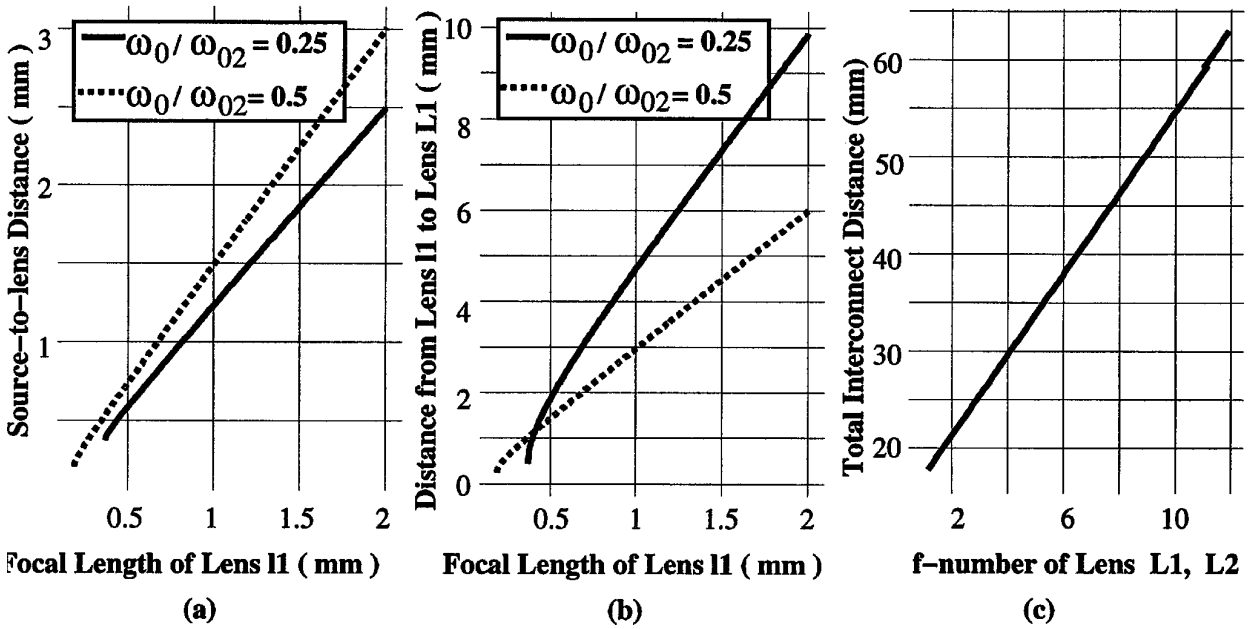

Fig. 7. (a) Interconnect distance $d1_{l1}$ versus focal length f_l of lens $l1$, (b) interconnect distance $d2_{l1}$ versus focal length f_l of lens $l1$, (c) total interconnect distance versus $(f/\#)_L$.

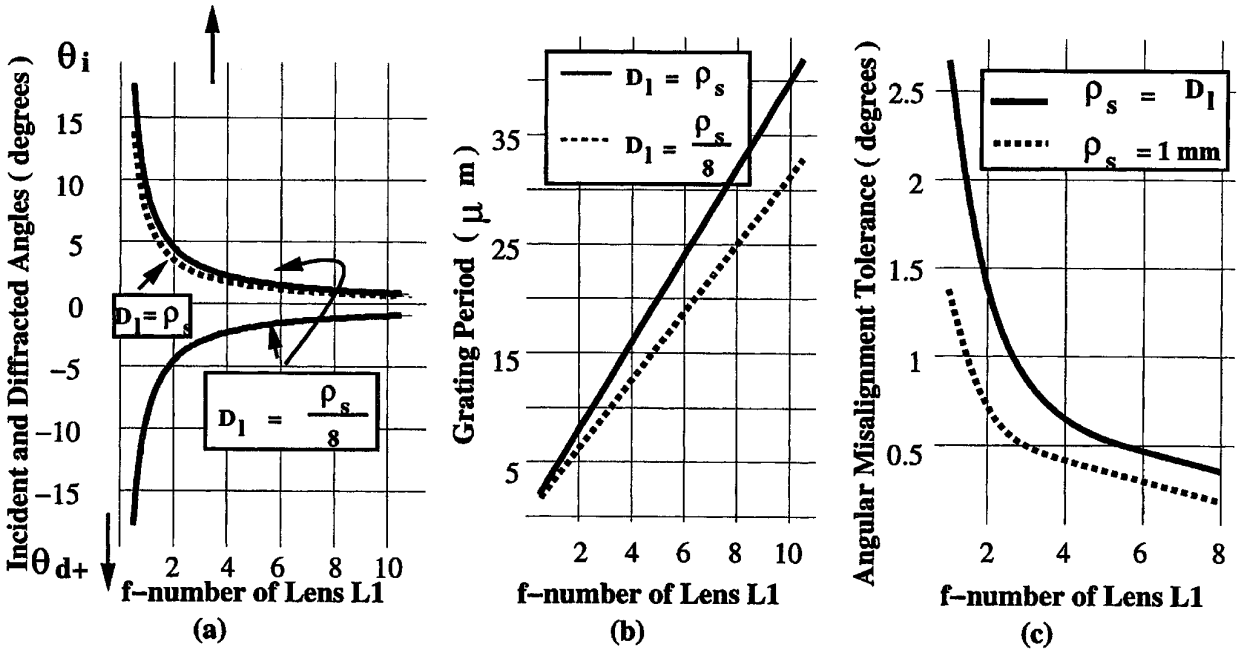

Fig. 8. (a) Angles of diffracted orders versus $(f/\#)_L$, (b) grating period Λ versus f-number $(f/\#)_L$ for different values of D_l, the diameter of lens $l1$, (c) angular misalignment tolerance versus f-number of lens L1 for different values of the lens diameter and separation.

From the geometry, the incident angle is defined by

$$\tan \theta_i = \frac{\rho_s}{2f_L} = \frac{\rho_s}{2(3\rho_s + D_l)(f/\#)_L}. \tag{15}$$

For the diffracted orders,

$$\tan \theta_{d0} = \tan \theta_i, \tag{16}$$

$$\tan \theta_{d+} = -\frac{\rho_s}{2f_L} = -\frac{\rho_s}{2(3\rho_s + D_l)(f/\#)_L}. \tag{17}$$

A graph of the incident angle θ_i, zeroth diffracted order θ_{d0}, and positive first diffracted order θ_{d+} versus the f-number of the lens $(f/\#)_L$ for $\rho_s = D_l$ is shown in Fig. 8(a). The grating period Λ can be calculated with Eqs. (14)–(17). A graph of the grating period Λ versus the f-number $(f/\#)_L$ is shown in Fig. 8(b) for different values of the diameter D_l of lens $l1$.

4. *Misalignment Sensitivity for the Free-Space Links*

An important parameter of free-space optical systems is the alignment tolerance, which can be considered as the component displacement or angular offset that can be permitted before significant power loss and cross talk occur. Alignment tolerance increases reliability and reduces cost but the trade-off is signal density.

A. Lateral Misalignment. Lateral misalignment of the VCSEL and lens $l1$ of ΔL_y with respect to the detector and lens $l2$ produces an angular displacement of the incident beam on the hologram. For the zeroth- and first-order diffracted beams, the displacement on lens $l2$ is a lateral shift of the same magnitude ΔL_y in opposite directions because one angle is negative of the other.

For a clipping ratio $k_l = 1.52$, 1% of the power is lost. Thus a lateral misalignment of $r_l - 1.52\omega_l = 2.12\omega_l - 1.52\omega_l = 0.6\omega_l$ can be tolerated at lens $l2$, while losing only 1% of the power, where r_l is the radius of lens $l2$ and ω_l is the radius of the spot size on the lens.

For the parameters in Table 2, $\Delta L_y = 72.92$ μm.

Table 2. Calculated System Parameters for the Free-Space Links in the OMMH

System Parameter	Symbol	Value
Wavelength	λ	0.85 μm
Source spot radius	ω_0	5 μm
Radius of beam on lens $l1$	ω_{l1}	121.53 μm
Diameter of lenses $l1$, $l2$	D_l	520 μm
Diameter of lenses L1, L2	D_L	2.08 mm
Focal length of lenses $l1$, $l2$	f_l	1.5 mm
Focal length of lenses L1, L2	f_L	10.16 mm
Clipping ratio of lens $l1$	k_l	2.12
f-number of lens L1	$(f/\#)_L$	5
Source-to-lens distance	$d1_{l1}$	2.244 mm
Lens $l1$ to lens L1 distance	$d2_{l1}$	4.477 mm
Grating period	Λ	17.05 μm
Hologram incident angle	θ_i	1.43°
Zeroth order	θ_{d0}	1.43°
Positive first order	θ_{d+}	4.29°
Negative first order	θ_{d-}	−1.43°
Detector diameter	$2r_d$	20 μm
Detector-to-detector spacing	ρ_d	520 μm
System efficiency	η_{sys}	0.085
System fan-out for hypercube	N	5

B. Angular Misalignment. Because the hologram is the component most sensitive to angular misalignments in the system, its tolerance would be used to characterize the system's angular misalignment sensitivity. For the hologram that is angularly misaligned, the sensitivity of the diffracted beam angle to angular variations of the reconstructed beam can be determined with the grating equation:

$$\theta_d = \sin^{-1}\left[\frac{m\lambda}{\Lambda} - \sin(\theta_i)\right]. \tag{18}$$

To maintain minimum power loss, the lateral displacement of the beam spot on lens $l2$ that is due to a new diffracted angle θ_d' should not exceed $0.6\omega_l$, as discussed above. This requirement places maximum tolerances on the angles of the diffracted orders that could be calculated from

$$|f_L(\tan\theta_d - \tan\theta_d')| \le 0.6\omega_l. \tag{19}$$

A graph of the misalignment tolerance versus the *f*-number of lens L1 is shown in Fig. 8(c) for different values of the spacing ρ_s. For a spacing $\rho_s = D_l = 520$ μm, an *f*-number of 4 implies an angular misalignment tolerance of 0.66°. Increasing the spacing to $\rho_s = 1$ mm implies an angular misalignment tolerance of 0.46°.

C. Longitudinal Misalignment. Longitudinal misalignment of the VCSEL and collimating lens with the detector and focusing lens causes the collimated beam waist incident upon lens L1 and subsequently leaving lens L2 to be of a larger radius. The resulting spot size on the focusing lens is therefore larger. Obtaining 99% of the light, using the clipping ratio of $k = 1.52$, would impose the following requirement on the expanded beam-spot radius ω_l':

$$\omega_l' \le \frac{r_l}{1.52} = \frac{2.12\omega_l}{1.52} = 1.39\omega_l. \tag{20}$$

A maximum spot size of 168.93 μm, from the parameters of Table 2, implies a maximum longitudinal misalignment tolerance of 1.755 mm.

D. Chromatic Sensitivity. Chromatic sensitivity that is due to the manufacturing tolerances in the wavelength of the source will cause the beam-waist diameter to change [see Eq. (1)]. The maximum spot-size radius on the lens that permits only a 1% loss is $1.39\omega_l$, as discussed above. The change in angular position of the diffracted beam will cause a lateral misalignment of the diffracted spot on the focusing lens. Assuming $\lambda = 0.85$ μm $\pm \Delta\lambda$, ω_l can increase to 168.93 μm, with parameters from Table 2. This implies that $\Delta\lambda = 0.33$ μm can be tolerated. Typical values of $\Delta\lambda$ are 50 nm. Typical wavelengths of commercially available VCSEL's are in the range 750–1050 nm. The implication of this is that all commercially available VCSEL's can be used in the proposed system.

Chromatic variations will also affect the angle of the diffracted beam from the hologram. Differentiating Eq. (18) while keeping θ_i constant yields

$$d\theta_d = \frac{m\,d\lambda}{\Lambda\cos\theta_d}. \tag{21}$$

The angular position of the zeroth order is not affected by chromatic variations. For $\Delta\lambda = 0.33$ μm, $d\theta_d = \pm 0.019°$ respectively for the positive and negative first orders. This corresponds to a resultant lateral displacement on lens $l2$ of ± 17.25 μm, which is 1 order of magnitude less than the total lateral misalignment tolerance of 72.92 μm. Thus chromatic variations of the diffracted beams from the hologram cause negligible power loss (<1%).

E. Modeling the Fiber-Based Links in the Optical Multimesh Hypercube

The mesh links of plane L and plane R are identical because the system is symmetrical and space invariant; as such, we consider only one plane. The conceptual view of the mesh links in the sample OMMH is shown in Fig. 4. Nodes with same addresses on different hypercubes are connected in a torus fashion. Thus {**n**0, **n**8, **n**16, **n**24} are in the same torus, as are, similarly, {**n**3, **n**11, **n**19, **n**27}, {**n**5, **n**13, **n**21, **n**29}, and {**n**6, **n**14, **n**22, **n**30}. A conceptual view of the proposed model for the interconnect links in one mesh is shown in Fig. 9. In reality, all sources would be grouped together so that VCSEL arrays and detector arrays could be used. The diagram here is used just to show the connectivity. Microlenses are used to couple light into the fiber and the detector arrays. Commercial means for connecting VCSEL's, fiber, and detectors are available. Each node in the mesh has four connections. The most simple and feasible solution is to have a dedicated VCSEL and detector for each connection. This method eliminates the problems associated with beam splitting if a single source is used (increased cross talk, increased required laser power, decreased link efficiency that is due to the fan-out, increased power dissipation and cooling problems, added volume that is due to the beam splitters, and the misalignment tolerances that are due to the increased number of components in the system). Because the connections are space variant because of the wraparound connections on the meshes, fiber ribbons or 2 − D fiber bundles are the most obvious interconnect medium.

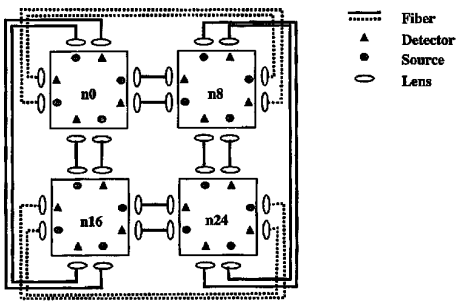

Fig. 9. Model for the mesh interconnects.

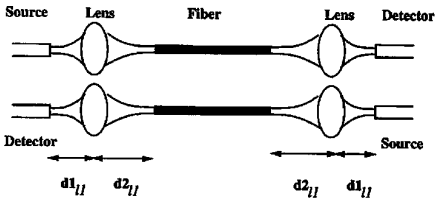

Fig. 10. Model of a single bidirectional link for the mesh interconnects.

Moreover, the use of four VCSEL's and four detectors on each node allows us to use commercially available fiber interconnects (Motorola's Optobus) for a physical demonstration of the mesh links. Each VCSEL and detector are represented by pinouts on the Optobus chip and thus can be modulated separately to do processing on individual nodes. More importantly, there will be no contention if all four neighbors need to communicate with a single node.

1. Beam Propagation through the Model

A simplified model for a single bidirectional link in the mesh is shown in Fig. 10. For optimum coupling to the fiber, the beam-spot radius incident upon the fiber in relation to the fiber core radius is given in Eq. (3). Geometric considerations require that the diameter of the lens $l1$ be such that four lenslets in the mesh would fit into one lenslet of the hypercube for packaging considerations. When the diameter of the lenslet and $k = 2.12$ are used in Eqs. (1)–(3), the distances $d1_{l1}$, $d2_{l1}$ and the focal length f_l of the coupling lens could be determined.

2. Optical Efficiency of the Fiber Links

The optical link efficiency for fiber interconnects depends on length-dependent attenuation $\Gamma(d)$, source-to-fiber coupling η_{sf}, and fiber-to-detector coupling η_{fd}. The efficiency η_{sys} of a fiber of length d is thus given by

$$\eta_{sys} = \eta_{fd}\eta_{sf}\Gamma(d), \tag{22}$$

$$\Gamma(d) = \log^{-1}(-\alpha_d d/10), \tag{23}$$

and α_d is the fiber attenuation loss in decibels per unit length.

3. Misalignment Sensitivity for the Fiber Links

We assume step-index fibers for which the numerical aperture is constant across the end face of the fiber and also that there is a uniform modal power distribution in the fiber. Using the power budget of Table 3, Eq. (10), and RZ coding, we plot the bit rate $(1/2\tau)$ versus misalignment in the subsections below to show a direct relation between power loss and bit rate by using single-mode and multimode fibers.

A. Lateral Misalignment. The lateral offset presents the most serious misalignment. If the core radius is a and the lateral offset of the center of the fiber core from the optic axis is ΔL_{lat}, then the loss in decibels for single-mode fibers is given by[14]

$$L_{lat} = -10 \log\left\{\exp\left[-\left(\frac{\Delta L_{lat}}{\omega_f}\right)^2\right]\right\}. \tag{24}$$

For multimode fibers, the loss in decibels is given by

$$L_{lat} = -10 \log\left\{\frac{2}{\pi}\cos^{-1}\left(\frac{\Delta L_{lat}}{2a}\right) - \frac{\Delta L_{lat}}{\pi a}\left[1 - \left(\frac{\Delta L_{lat}}{2a}\right)^2\right]^{1/2}\right\}. \tag{25}$$

A graph of the bit rate versus the lateral misalignment is shown in Fig. 11(a) for single and multimode fibers.

B. Angular Misalignment. For angular misalignment in single-mode fibers, the loss at a wavelength λ is given by[14]

$$L_{ang} = -10 \log\left\{\exp\left[-\left(\frac{\pi n_2 \omega_f \Delta\theta}{\lambda}\right)^2\right]\right\}, \tag{26}$$

where n_2 is the refractive index of the cladding and $\Delta\theta$ is the angular misalignment in radians. For multimode fibers, the loss is given by

$$L_{ang} = -10 \log\left(1 - \frac{\tan\Delta\theta}{\pi \mathrm{NA}}\right). \tag{27}$$

A graph of the bit rate versus the angular misalignment is given in Fig. 11(b) for single and multimode fibers.

C. Longitudinal Misalignment. The longitudinal loss for single-mode fibers is given by[14]

$$L_{long} = -10 \log \frac{4(4Z^2 + 1)}{(4Z^2 + 2)^2 + 4Z^2}, \tag{28}$$

where

$$Z = \frac{\Delta L_{long}\lambda}{2\pi n_2 \omega_f^2} \tag{29}$$

and ΔL_{long} is the longitudinal misalignment.

For multimode fibers, the loss is given by

$$L_{long} = -10 \log\left(1 - \frac{\Delta L_{long}\mathrm{NA}}{4a}\right). \tag{30}$$

Table 3. Typical Fiber-Link Power Budget

Parameter	Value	dBm
Laser power P_l	0.85 mW	−0.706
Laser-to-fiber coupling loss (η_c)		−2
Attenuation loss		Negligible
Bending loss		−3
Fiber-to-detector coupling loss		−3
Engineering margin		−5
Power incident upon detector (P_d)	42.599 μW	−13.706
Detector quantum efficiency (η_d)	0.877	−0.57
Photocurrent at receiver (i_d)	25.56 μA	

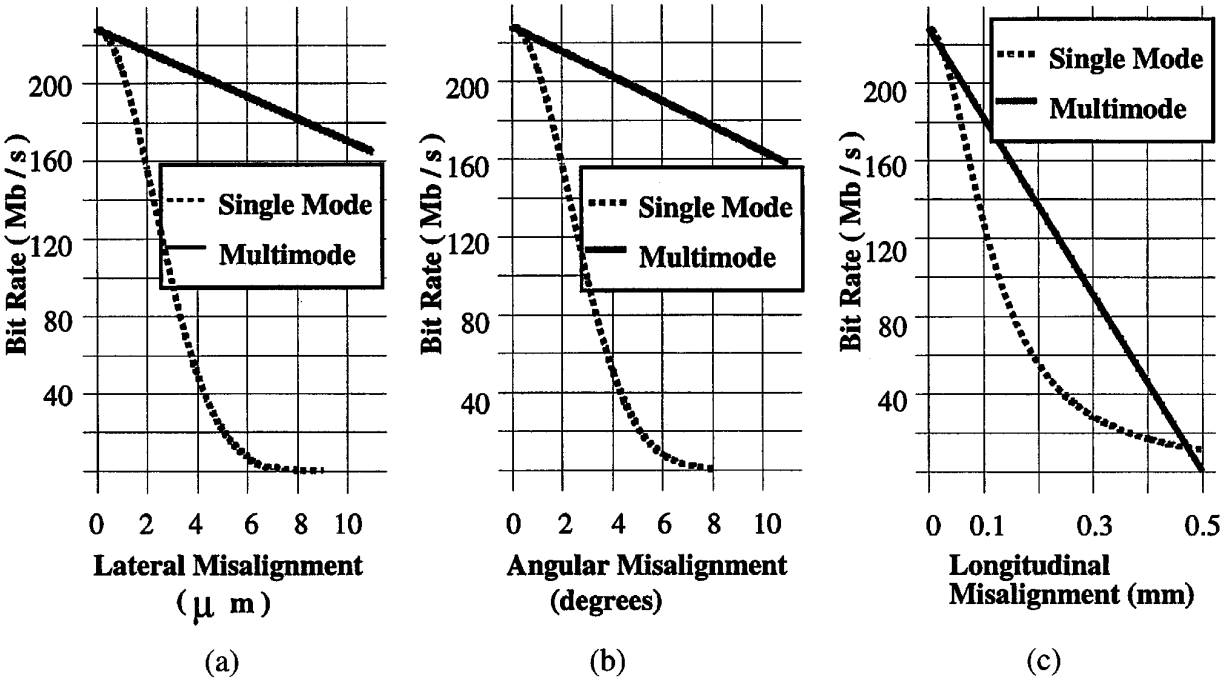

Fig. 11. (a) Bit rate versus lateral misalignment for single and multimode fibers, (b) bit rate versus angular misalignment for single and multimode fibers, (c) bit rate versus longitudinal misalignment for single and multimode fibers.

A graph of the bit rate versus the longitudinal misalignment for single and multimode fibers is shown in Fig. 11(c).

F. System Parameters and Power Budget

Based on the geometry with power loss considerations, Table 2 gives the calculated system parameters for the free-space links and Table 4 gives the same for the fiber links. A power budget for the free-space links is shown in Table 5. For a laser output power of 0.85 mW, 72.243 μW is incident upon the detector. A power budget for the fiber links is shown in Table 3. For 0.85-mW laser output power, only 42.59 μW is incident upon the detector. A graph of output laser power versus the power incident upon the detector is shown in Fig. 2(c).

Table 4. System Parameters for the Fiber Links in the OMMH

System Parameter	Symbol	Single Mode	Multimode
Core radius of fiber	a	3 μm	25 μm
Core refractive index	n_1	1.4574	—
Cladding refractive index	n_2	1.4529	—
Numerical aperture of fiber	NA	0.11	0.2
Mode field radius	ω_f	3.25 μm	16.25 μm
Focal length of lenses $l1, l2$	f_l	448 μm	877 μm
Source-to-lens distance	$d1_{l1}$	1.13 mm	1.13 mm
Lens $l1$ to fiber distance	$d2_{l1}$	737 μm	3.251 mm
Wavelength	λ	0.85 μm	
Source spot radius	ω_0	5 μm	
Detector diameter	$2r_d$	20 μm	
Clipping ratio of lens $l1$	k_l	2.12	
Diameter of lenses $l1, l2$	D_l	130 μm	
Radius of beam on lens $l1$	ω_{l1}	61.34 μm	
Detector-to-detector spacing	ρ_d	130 μm	
System efficiency	η_{sys}	0.05	

5. Discussion

The total interconnect distance is 3.38 cm for an f-number of 5 from Fig. 7(c). There are numerous trade-offs in choosing an appropriate f-number for lenses L1 and L2 in the system. First, larger f-numbers imply reduced aberrations. As the f-number decreases, the interconnect distance also decreases, as shown in Fig. 7. Larger f-numbers imply smaller angles, as shown in Fig. 8(a), and increased grating periods, as shown in Fig. 8(b), but also imply reduced angular misalignment tolerance, as shown in Fig. 8(c). The hybrid system for the hypercube links thus reduces aberrations, but the hologram recording angles limit the f-number. This problem can be alleviated by the use of diffractive optic elements for the microlenses.

Table 5. Free-Space Link Power Budget

Parameter	Value	dBm
Laser power P_l	0.85 mW	−0.706
Coupling efficiency of lens $l1$ (η_c)	0.999	-4.34×10^{-3}
Hologram coupling efficiency ($\eta_h/5$)	0.17	−7.696
Coupling efficiency of lens $l2$ (η_c)	0.999	-4.34×10^{-3}
Coupling efficiency into detector (η_{cd})	0.9996	-1.74×10^{-3}
Engineering margin		−3
Power incident upon detector P_d	72.243 μW	−11.412
Detector quantum efficiency η_d	0.877	−0.57
Photocurrent at receiver i_d	43.35 μA	

From Fig. 2(b), higher bit rates require more laser power, but capacitances at the receiver end drive the bit rates lower. Thus the laser output power of commercially available VCSEL's is adequate for our purpose. For the free-space links, more power is needed than for the fiber links, as shown in Fig. 2(b), because of the fan-out for the space-invariant imaging. We observe from Fig. 3(a) that, for detector capacitances of $\approx$14 fF in our system, the bit rate is limited to 368 Mbits/s for the free-space hypercube links and $\sim$228 Mbits/s for the mesh links.

For massively parallel processing systems, the transmitting planes for each hypercube link will be composed of an $N \times N$ pixel array in which each transmitting pixel contains a multiple-wavelength VCSEL array. Each laser in a pixel emits light at a different wavelength equally spaced apart. WDM pixels can be fabricated by the alteration of existing multiple-wavelength VCSEL technology. The pixel area would be dominated by the driver electronics and not by the relatively small VCSEL array; thus adding more lasers would not alter the pixel density on the chip. The detection plane would also have N^2 pixels, each containing a PIN-PD array with a large spectral response and wavelength-selective filters to filter out the n wavelengths (node degree of the hypercube). Using 16-bits bit-parallel transmission implies that 4×4 VCSEL arrays are needed on each node, yielding a bit rate of 5.88 Gbits/s for the free-space links and 3.65 Gbits/s for the fiber links. From the pixel density versus laser output power curve in Fig. 2(a), 16 pixels/cm^2 is feasible.

The limitation, however, would be the number of available wavelengths. Wavelength separations of $\Delta\lambda = 0.3$ nm over a range of 430 nm have been reported. For more practical values of $\Delta\lambda = 4.5$ nm, a range of 300 nm would imply $\sim$66 usable wavelengths. For bit-serial transmission, an OMMH $(l, m, 7)$ would be possible over the range of commercially available wavelengths. For 16-bits bit-parallel transmission, $n = 3$ is possible. As VCSEL technology advances with smaller $\Delta\lambda$ separations, higher-order OMMH's will be possible.

The predicted system size when bit-serial transmission is used for the free-space links for the sample OMMH (2, 2, 3) is 4.16 mm $\times$ 4.16 mm $\times$ 3.38 cm. For 16-bits bit parallel per node, the predicted system size is 1.04 cm $\times$ 1.04 cm $\times$ 3.38 cm. Implementing bidirectional communication from plane L to plane R requires twice this volume.

From the curves of Figs. 11(a)–11(c) with a 2-μm lateral misalignment, bit rates of over 200 Mbits/s are still achievable with multimode fibers. For single-mode fibers, however, the bit rate drops to 160 Mbits/s. However, from Table 4, multimode fibers have longer interconnection distances, focal lengths, and diameters. Thus more compact systems are possible with single-mode fibers but the trade-off is misalignment sensitivity and bit rate.

In terms of cross talk, the system has been studied for < -20 dB. We can reduce the system size by allowing more cross talk, but the signal-to-noise ratio will have to increase to achieve a desired BER. This would require more power, which entails expensive cooling techniques for heat removal.

6. Conclusions

We have presented a feasibility study of a scalable optical interconnection network (OMMH) for massively parallel processing systems. Its optical implementation appears quite feasible based on the modeling predictions in terms of bit rate, power budget, component and system size, receiver design, interconnect distance, link efficiency, pixel density, and misalignment sensitivity. Finally, all our calculated geometric and system parameters are within the ranges of commercially available components.

This research was supported by National Science Foundation grant MIP 9310082.

References

1. A. Louri and H. Sung, "Efficient implementation methodology for three-dimensional space-invariant hypercube-based free-space optical interconnection networks," Appl. Opt. **32,** 7200–7209 (1993).
2. A. Louri and H. Sung, "Scalable optical hypercube-based interconnection network for massively parallel computing," Appl. Opt. **33,** 7588–7598 (1994).
3. A. Louri and H. Sung, "An optical multi-mesh hypercube: a scalable optical interconnection network for massively parallel computing," J. Lightwave Technol. **12,** 704–716 (1994).
4. S. Tang, R. T. Chen, L. Garrett, D. Gerold, and M. M. Li, "Design limitations of highly parallel free-space optical interconnects based on arrays of vertical cavity surface-emitting laser diodes, microlenses, and photodetectors," J. Lightwave Technol. **12,** 1971–1975 (1994).
5. J. Neff, "Optical interconnects based on two-dimensional VCSEL arrays," in *IEEE Proceedings of the First International Workshop on Massively Parallel Processing Using Optical Interconnections* (Institute of Electrical and Electronic Engineers, New York, 1994), pp. 202–212.
6. G. Olbright, "VCSELs could revolutionize optical communications," Photon. Spectra, **29,** 98–101 (1995).
7. S. Kawai, H. Kurita, and I. Ogura, "Optical switching networks using free-space wavelength-division multiplexing interconnections," Inst. Electron. Inf. Commun. Eng. (Jpn) Trans. Electron. **E78-C,** 81–84 (1995).
8. I. Ogura, K. Kurihara, S. Kawai, M. Kahita, and K. Kasahara, "A multiple wavelength vertical-cavity surface-emitting laser (VCSEL) array for optical interconnection," Inst. Electron. Inf. Commun. Eng. (Jpn) Trans. Electron. **E78-C,** 22–27 (1995).
9. A. E. Willner, C. H. Chang-Hasnain, and J. E. Leight, "2-D WDM optical interconnections using multiple-wavelength VCSELs for simultaneous and reconfigurable communication among many planes," IEEE Photon. Technol. Lett. **5,** 838–841 (1993).
10. Y. Motegi and A. Takai, "Optical interconnection modules utilizing fiber-optic parallel transmission to enhance information throughput," Hitachi Rev. **43,** 79–82 (1994).
11. A. Takai, H. Abe, and T. Kato, "Subsystem optical interconnections using long wavelength laser diode arrays and single-mode fiber arrays," J. Lightwave Technol. **12,** 260–270 (1994).
12. G. Nakagawa, K. Miura, M. Makiuchi, and M. Yano, "Highly efficient coupling between LD array and optical fiber array using Si microlens array," IEEE Photon. Technol. Lett. **5,** 1056–1058 (1993).

13. F. B. McCormick, F. A. P. Tooley, T. J. Cloonan, J. M. Sasian, and H. S. Hinton, "Optical interconnections using microlens arrays," Opt. Quantum Electron. **24,** S465–S477 (1992).
14. D. Marcuse, "Loss analysis of single-mode fiber splices," Bell Syst. Tech. J. **56,** 703–718 (1977).
15. B. Acklin and J. Jahns, "Packaging considerations for planar optical interconnection systems," Appl. Opt. **33,** 1391–1397 (1994).
16. R. D. Smith and S. D. Personick, "Receiver design for optical fiber communication systems," in *Semiconductor Devices for Optical Communications,* H. Kressel, ed. (Springer-Verlag, Heidelberg, 1987), Chap. 4.
17. T. V. Moui, "Receiver design for high-speed optical fiber systems," J. Lightwave Technol. 243–267 (1984).
18. F. B. McCormick, "Free-space interconnection techniques," in *Photonics in Switching: Volume II, Systems,* J. E. Midwinter, ed. (Academic, New York, 1993), Chap. 4.
19. S. Sinzinger and J. Jahns, "Variations of the hybrid imaging concept for optical computing applications," in *Optical Computing,* Vol. 10 of 1995 OSA Technical Digest Series (Optical Society of America, Washington, D.C., 1995), pp. 183–185.
20. J. Jahns, F. Sauer, B. Tell, K. Brown-Goebeler, A. Feldblum, W. Townsend, and C. Nijander, "Parallel optical interconnections using surface-emitting microlasers and a hybrid imaging system," Opt. Commun. **109,** 328–337 (1994).
21. R. S. L. J. Camp and M. R. Feldman, "Guided-wave and free-space optical interconnects for parallel processing systems: a comparison," Appl. Opt. **33,** 6168–6180 (1994).